

# Numerical model of elastic laminated glass beams under finite strain

ALENA ZEMANOVÁ<sup>1</sup>, JAN ZEMAN<sup>1,2</sup>, AND MICHAL ŠEJNOHA<sup>1</sup>

<sup>1</sup>*Department of Mechanics, Faculty of Civil Engineering, Czech Technical University in Prague, Thákurova 7, 166 29 Prague 6, Czech Republic*

<sup>2</sup>*Centre of Excellence IT4Innovations, VŠB-TU Ostrava, 17. listopadu 15/2172 708 33 Ostrava-Poruba, Czech Republic*

## Abstract

Laminated glass structures are formed by stiff layers of glass connected with a compliant plastic interlayer. Due to their slenderness and heterogeneity, they exhibit a complex mechanical response that is difficult to capture by single-layer models even in the elastic range. The purpose of this paper is to introduce an efficient and reliable finite element approach to the simulation of the immediate response of laminated glass beams. It proceeds from a refined plate theory due to Mau (1973) [*Journal of Applied Mechanics-Transactions of the ASME* 40, 606–607], as we treat each layer independently and enforce the compatibility by the Lagrange multipliers. The finite element discretization at the layer level adopts the finite-strain shear deformable element proposed by Ibrahimbegović and Frey (1993) [*International Journal for Numerical Methods in Engineering* 36, 3239–3258]. The resulting system is solved by the Newton method with consistent linearization. By comparing the model predictions against available experimental data, analytical methods and two-dimensional finite element simulations, we demonstrate that the proposed formulation is reliable and provides accuracy comparable to the detailed two-dimensional finite element analyses. As such, it offers a convenient basis to incorporate more refined constitutive description of the interlayer.

**Keywords** laminated glass; finite-strain Reissner beam theory; finite element method; Lagrange multipliers

## 1 Introduction

Due to present trends in architecture and photovoltaics, the use of structural glass expands from traditional window panes to large-area surfaces, roof and floor systems, columns or staircases. This leads to an increased emphasis on the safety and the mechanical performance of structural members made of glass. Perhaps the most popular material system meeting these criteria is laminated glass. It is a composite structure produced by bonding multiple layers of glass together with a transparent plastic interlayer, typically made of polyvinyl butyral (PVB) foil [10, 25]. The interlayer absorbs the energy impact, thereby resisting the glass penetration, and keeps the layers of glass bonded when fractured.

Laminated glass units exhibit a complex mechanical response, as a consequence of their heterogeneity. Namely, the contrast in elastic properties between glass and the interlayer typically exceeds three orders of magnitude, which renders classical laminate theories inapplicable since the glass layers deform mainly due to bending, whereas the interlayer experiences a pure shear. Moreover, PVB is a viscoelastic material exhibiting a high sensitivity to temperature changes, e.g. [5]. Finally, glass structures are very slender and must be analyzed using geometrically non-linear theories.

In practical applications, the behavior of laminated glass units is often approximated by an equivalent, geometrically linear, single-layer elastic system. According to the performance of the interlayer, we distinguish the layered case, in which the structure responds as an assembly of independent layers, and the monolithic model with thickness equal to the combined thickness of glass layers and interlayer. This approach was pioneered by experimental studies of Behr et al. [3], who demonstrated that the degree of coupling due to the interlayer is significant at room temperatures and ceases at elevated temperatures. This was extended later in [4] to quantify the validity of the monolithic approximation in terms of temperature range and load duration. Norville et al. [22] further refined these results by studying the shear coupling around the transition temperature of the interlayer and demonstrated that the performance of laminated units exceeds the layered limit even above the transition point. Vallabhan et al. [27] introduced a notion of the strength factor as a ratio between the maximal principal strength in the equivalent monolithic unit and the laminated system and demonstrated that it can reach values smaller than one for cases of practical interest. They attributed this to the effects of geometrical non-linearity which become significant earlier for the laminated units than for the monolithic ones. These developments have been recently put on a rigorous basis by Galuppi and Royer-Carfagni [8], who derived explicit variationally-based formulas for deflection- and stress-equivalent thicknesses of monolithic systems.

Apart from experimental results, the validity of simplified models was assessed by several analytical studies. When restricting our attention to planar glass beams, the first study is due to Hooper [12], who derived a three-layer model under small deflections and presented the solution for the four point bending setup with different duration of loading and ambient temperatures. Later, Aşık and Tescan [2] extended this model to account for large deflections and demonstrated that they significantly contribute to the overall response when the normal forces start to develop, see also Section 5 for a concrete example. In the linear setting, Ivanov [17] proposed a procedure for thickness optimization of triplex glasses and Foraboschi [7] demonstrated that the empirical rules proposed by Behr et al. [4] may lead to unsafe designs. Recently, Schultze et al. [24] performed an experimental-analytical study into the response of the laminated structures used in photovoltaic applications under three-point bending.

Even though the analytical approaches give valuable insight into the behavior of laminated glass structures, they still suffer from two major limitations. First, the only closed-form solutions we are aware of hold only in the absence of membrane effects. In the opposite case, the governing differential equations have to be discretized anyhow and the discrete problem is often solved using the problem-specific procedures that experience convergence problems, e.g. [1]. Second, the analytical approaches require the interlayer to be replaced by an equivalent elastic material, with properties adjusted to the loading duration and ambient temperature. As shown by Galuppi and Royer-Carfagni [9], this approach leads to significant errors in local stresses and strains.

With these limitations in mind, we proposed in [28] a numerical approach to the analysis of laminated glass beams based on a refined laminate theory due to Mau [21]. In this framework, the structure is seen as an assembly of shear-deformable layers with independent kinematics and the inter-layer interaction is enforced by the Lagrange multipliers. Due to the modular format, each layer can be discretized by appropriate finite elements, and the resulting system is ideally suited for the deployment of efficient iterative solvers [19] or multi-scale modeling at the layer level [26].

In this paper, we extend our previous results [28], valid in small strains, to the finite-strain regime. To this purpose, each layer is modeled by the Reissner beam theory [23], briefly summarized in Section 2 in a variational format. Discretization in Section 3 is based on a robust finite element formulation proposed by Ibrahimbegović and Frey in [14] and later applied, e.g., to discrete materials modeling [13], or optimal control and design of structures [15]. In Section 4, we derive the discretized system arising from the optimality conditions of the associated constrained optimization problem, and perform its solution by the Newton method. Accuracy

of the implementation is examined in Section 5 by verifying our results against data presented by Aşık and Tescan [2]. To make the paper self-contained, in Appendix A we collect the details on tangent operators needed when implementing the Newton method. Note that this paper is focused on the immediate elastic response of laminated structures. The effect of time-dependent viscous properties of the interlayer will be discussed independently and in more details in a forthcoming publication.

The following nomenclature is used in the text. Scalar quantities are denoted by lightface letters, e.g.  $a$ , and the bold letters are reserved for matrices, e.g.  $\mathbf{a}$  or  $\mathbf{A}$ .  $\mathbf{A}^\top$  standardly stands for the matrix transpose and  $\mathbf{A}^{-1}$  for the matrix inverse. The subscript in parentheses, e.g.  $a^{(i)}$ , is used to emphasize that the variable  $a$  is associated with the  $i$ -th layer.

## 2 Model formulation

In our setting, a glass beam is considered as an assembly of three beams of identical length  $L$ , with the cross-section dimensions  $b \times h^{(i)}$ . Each layer is considered to behave according to the Reissner finite-strain beam theory [23], i.e. we assume that cross-sections remain planar, but not necessarily perpendicular to the deformed beam curve, and that the distance of a point at the cross-section from the centerline remains unchanged. For the  $i$ -th layer, the coordinates of a point in the deformed configuration can be determined as, Figure 1,

$$x^{(i)}(X^{(i)}, Z^{(i)}) = O_X^{(i)} + X^{(i)} + u_0^{(i)}(X^{(i)}) + \sin(\varphi^{(i)}(X^{(i)}))Z^{(i)}, \quad (1a)$$

$$z^{(i)}(X^{(i)}, Z^{(i)}) = O_Z^{(i)} + w_0^{(i)}(X^{(i)}) + \cos(\varphi^{(i)}(X^{(i)}))Z^{(i)}, \quad (1b)$$

where  $O_X^{(i)}$  and  $O_Z^{(i)}$  stand for the coordinates of the beam origin,  $X^{(i)}$  is the ordinate of a cross-section,  $u_0^{(i)}$  and  $w_0^{(i)}$  are centerline displacements measured in the global coordinate system,  $\varphi^{(i)}$  is the rotation of the cross-section, and  $Z^{(i)}$  is the coordinate measured along the cross-section. The inter-layer interaction is ensured via the geometric continuity conditions at the interfaces between the layers ( $i = 1, 2$ )

$$x^{(i)}(X^{(i)}, \frac{1}{2}h^{(i)}) - x^{(i+1)}(X^{(i)}, -\frac{1}{2}h^{(i+1)}) = 0, \quad (2a)$$

$$z^{(i)}(X^{(i)}, \frac{1}{2}h^{(i)}) - z^{(i+1)}(X^{(i)}, -\frac{1}{2}h^{(i+1)}) = 0. \quad (2b)$$

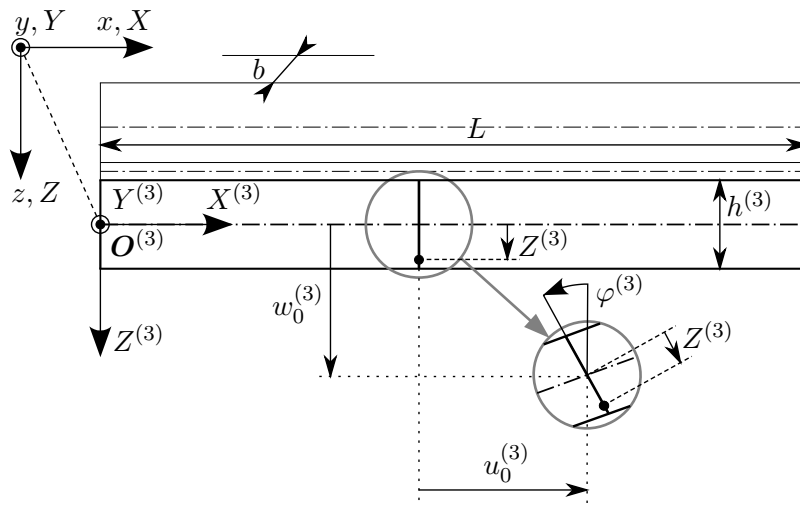


Figure 1: Kinematics of a cross section of the bottom layer of a laminated beam ( $i = 3$ ).

As demonstrated, e.g. by Ibrahimbegović and Frey [14] and Irschik and Gerstmayr [16], the Reissner beam theory can be consistently derived from the continuum framework by the

Biot-type strain tensors for the kinematics parametrization (1). To this purpose, we use the deformation gradient in the form

$$\mathbf{F}^{(i)}(X^{(i)}, Z^{(i)}) = \begin{bmatrix} \frac{\partial x^{(i)}}{\partial X^{(i)}} & \frac{\partial x^{(i)}}{\partial Z^{(i)}} \\ \frac{\partial z^{(i)}}{\partial X^{(i)}} & \frac{\partial z^{(i)}}{\partial Z^{(i)}} \end{bmatrix} (X^{(i)}, Z^{(i)}), \quad (3)$$

with individual entries provided by

$$F_{11}^{(i)} = 1 + \frac{du_0^{(i)}(X^{(i)})}{dX^{(i)}} + \cos(\varphi^{(i)}(X^{(i)})) \frac{d\varphi^{(i)}(X^{(i)})}{dX^{(i)}} Z^{(i)}, \quad (4a)$$

$$F_{12}^{(i)} = \sin(\varphi^{(i)}(X^{(i)})), \quad (4b)$$

$$F_{21}^{(i)} = \frac{dw_0^{(i)}(X^{(i)})}{dX^{(i)}} - \sin(\varphi^{(i)}(X^{(i)})) \frac{d\varphi^{(i)}(X^{(i)})}{dX^{(i)}} Z^{(i)}, \quad (4c)$$

$$F_{22}^{(i)} = \cos(\varphi^{(i)}(X^{(i)})). \quad (4d)$$

The deformation gradient  $\mathbf{F}^{(i)}$  admits a multiplicative decomposition

$$\mathbf{F}^{(i)}(X^{(i)}, Z^{(i)}) = \mathbf{R}^{(i)}(X^{(i)}) \mathbf{U}^{(i)}(X^{(i)}, Z^{(i)}), \quad (5)$$

where the rotation matrix of the  $i$ -th layer is given by, recall Figure 1,

$$\mathbf{R}^{(i)} = \begin{bmatrix} \cos(\varphi^{(i)}(X^{(i)})) & \sin(\varphi^{(i)}(X^{(i)})) \\ -\sin(\varphi^{(i)}(X^{(i)})) & \cos(\varphi^{(i)}(X^{(i)})) \end{bmatrix}, \quad (6)$$

and  $\mathbf{U}^{(i)}$  is follows from the inverse relation

$$\mathbf{U}^{(i)}(X^{(i)}, Z^{(i)}) = [\mathbf{R}^{(i)}(X^{(i)})]^{-1} \mathbf{F}^{(i)}(X^{(i)}, Z^{(i)}), \quad (7)$$

that provides

$$U_{11}^{(i)} = \cos(\varphi^{(i)}(X^{(i)})) \left( 1 + \frac{du_0^{(i)}(X^{(i)})}{dX^{(i)}} \right) - \sin(\varphi^{(i)}(X^{(i)})) \frac{dw_0^{(i)}(X^{(i)})}{dX^{(i)}} + \frac{d\varphi^{(i)}(X^{(i)})}{dX^{(i)}} Z^{(i)}, \quad (8a)$$

$$U_{12}^{(i)} = 0, \quad (8b)$$

$$U_{21}^{(i)} = \sin(\varphi^{(i)}(X^{(i)})) \left( 1 + \frac{du_0^{(i)}(X^{(i)})}{dX^{(i)}} \right) + \cos(\varphi^{(i)}(X^{(i)})) \frac{dw_0^{(i)}(X^{(i)})}{dX^{(i)}}, \quad (8c)$$

$$U_{22}^{(i)} = 1. \quad (8d)$$

Employing the definition of the Biot-type strain tensor, e.g. [18, Eq. (24.27)],

$$\mathbf{H}^{(i)}(X^{(i)}, Z^{(i)}) = \mathbf{U}^{(i)}(X^{(i)}, Z^{(i)}) - \mathbf{I}, \quad (9)$$

the non-zero strain components are given by

$$H_{11}^{(i)}(X^{(i)}, Z^{(i)}) = E^{(i)}(X^{(i)}) + K^{(i)}(X^{(i)}) Z^{(i)}, \quad H_{21}^{(i)}(X^{(i)}) = \Gamma^{(i)}(X^{(i)}), \quad (10)$$

where  $E^{(i)}$ ,  $K^{(i)}$  and  $\Gamma^{(i)}$  denote the generalized normal strain, pseudo-curvature and shear strain introduced by Reissner [23]:

$$\begin{aligned} E^{(i)} &= E(u_0^{(i)}, w_0^{(i)}, \varphi^{(i)}) \\ &= \cos(\varphi^{(i)}(X^{(i)})) \left( 1 + \frac{du_0^{(i)}(X^{(i)})}{dX^{(i)}} \right) - \sin(\varphi^{(i)}(X^{(i)})) \frac{dw_0^{(i)}(X^{(i)})}{dX^{(i)}} - 1, \end{aligned} \quad (11a)$$

$$\begin{aligned} \Gamma^{(i)} &= \Gamma(u_0^{(i)}, w_0^{(i)}, \varphi^{(i)}) \\ &= \sin(\varphi^{(i)}(X^{(i)})) \left( 1 + \frac{du_0^{(i)}(X^{(i)})}{dX^{(i)}} \right) + \cos(\varphi^{(i)}(X^{(i)})) \frac{dw_0^{(i)}(X^{(i)})}{dX^{(i)}}, \end{aligned} \quad (11b)$$

$$K^{(i)} = K(u_0^{(i)}, w_0^{(i)}, \varphi^{(i)}) = \frac{d\varphi^{(i)}(X^{(i)})}{dX^{(i)}}. \quad (11c)$$

It is useful to express these relations in a compact form

$$\mathbf{u}^{(i)}(X^{(i)}) = \begin{bmatrix} u_0^{(i)} \\ w_0^{(i)} \\ \varphi^{(i)} \end{bmatrix} (X^{(i)}), \quad \mathbf{E}^{(i)}(X^{(i)}) = \begin{bmatrix} E^{(i)} \\ \Gamma^{(i)} \\ K^{(i)} \end{bmatrix} (X^{(i)}), \quad (12)$$

and denote by  $\mathbf{E}(\mathbf{u})$  a mapping assigning the generalized strain measures to the generalized centerline displacements  $\mathbf{u}$  according to Eq. (11).

The model is completed by specifying the energy functionals associated with the deformation of the laminated beam. In particular, the internal energy of the  $i$ -th layer is provided by [14]

$$\Pi_{\text{int}}^{(i)}(\mathbf{E}^{(i)}) = \frac{1}{2} \int_0^L E^{(i)} A^{(i)} (E^{(i)}(X^{(i)}))^2 + G^{(i)} A_s^{(i)} (\Gamma^{(i)}(X^{(i)}))^2 + E^{(i)} I^{(i)} (K^{(i)}(X^{(i)}))^2 dX^{(i)}, \quad (13)$$

where  $E^{(i)}$  and  $G^{(i)}$  denote the Young and shear moduli, and  $A^{(i)} = bh^{(i)}$ ,  $A_s^{(i)} = \frac{5}{6}A^{(i)}$  and  $I^{(i)} = \frac{1}{12}b(h^{(i)})^3$  stand for the the cross-section area, effective shear area, and the second moment of area, respectively. The external energy due to loading acting at the  $i$ -th layer assumes the form

$$\Pi_{\text{ext}}^{(i)}(\mathbf{u}^{(i)}) = - \int_0^L w_0^{(i)}(X^{(i)}) \bar{f}_Z^{(i)}(X^{(i)}) dX^{(i)} - \sum_{p=1}^{n^{\text{p}(i)}} w_0^{(i)}(X_p^{(i)}) \bar{F}_Z^{(i)}(X_p^{(i)}), \quad (14)$$

where, for simplicity, we assume that the structure is subjected to the distributed loading with intensity  $\bar{f}_Z^{(i)}$  and to  $n^{\text{p}(i)}$  concentrated forces  $\bar{F}_Z^{(i)}$  acting at  $X_p^{(i)}$ . The total energy of the  $i$ -th layer is then given by

$$\Pi^{(i)}(\mathbf{u}^{(i)}) = \Pi_{\text{int}}^{(i)}(\mathbf{E}(\mathbf{u}^{(i)})) + \Pi_{\text{ext}}^{(i)}(\mathbf{u}^{(i)}), \quad (15)$$

and at the level of the whole structure it reads

$$\Pi(\mathbf{u}^{(1)}, \mathbf{u}^{(2)}, \mathbf{u}^{(3)}) = \sum_{i=1}^3 \Pi^{(i)}(\mathbf{u}^{(i)}). \quad (16)$$

### 3 Finite element discretization

It is convenient for the numerical treatment to discretize all layers identically with  $n^e$  elements per each layer; by  $\Omega_e^{(i)}$  we denote the  $e$ -th element of the  $i$ -th layer. The displacement fields at the element level are approximated as

$$u_0^{(i)}(x) \approx \mathbf{N}_e(x) \mathbf{d}_e^{u(i)}, \quad w_0^{(i)}(x) \approx \mathbf{N}_e(x) \mathbf{d}_e^{w(i)}, \quad \varphi^{(i)}(x) \approx \mathbf{N}_e(x) \mathbf{d}_e^{\varphi(i)} \quad \text{for } x \in \Omega_e^{(i)}, \quad (17)$$

where  $\mathbf{N}_e$  is the matrix of piecewise linear basis functions, and e.g.  $\mathbf{d}_e^{\varphi(i)} = [\varphi_{e,1}^{(i)}, \varphi_{e,2}^{(i)}]^\top$  collects the nodal rotations  $\varphi^{(i)}$ , cf. Figure 2.

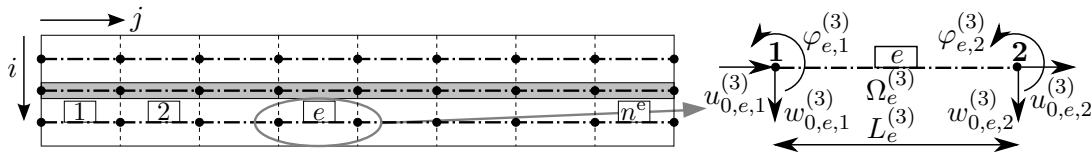


Figure 2: Scheme of discretization and element degrees of freedom.

Inserting the approximate fields (17) into the energy functionals (15) results in

$$\Pi_{\text{int}}^{(i)}(\mathbf{u}^{(i)}) \approx \sum_{e=1}^{n^e} \Pi_{\text{int},e}^{(i)}(\mathbf{d}_e^{(i)}), \quad \Pi_{\text{ext}}^{(i)}(\mathbf{u}^{(i)}) \approx \sum_{e=1}^{n^e} \Pi_{\text{ext},e}^{(i)}(\mathbf{d}_e^{(i)}) = - \sum_{e=1}^{n^e} \mathbf{d}_e^{(i)\top} \mathbf{f}_{\text{ext},e}^{(i)}, \quad (18)$$

where the matrix  $\mathbf{d}_e^{(i)}$  collects the nodal unknowns,

$$\mathbf{d}_e^{(i)} = \begin{bmatrix} u_{0,e,1}^{(i)} & w_{0,e,1}^{(i)} & \varphi_{e,1}^{(i)} & u_{0,e,2}^{(i)} & w_{0,e,2}^{(i)} & \varphi_{e,2}^{(i)} \end{bmatrix}^\top, \quad (19)$$

recall Figure 2, and  $\mathbf{f}_{\text{ext},e}^{(i)}$  stores the corresponding generalized nodal forces. As demonstrated in detail by Ibrahimbegović and Frey [14], the normal and shear locking even for the non-linear kinematics can be suppressed by adopting the selective one-point integration of the corresponding terms in (13). Thus, the approximate generalized strain measures (11) are taken as element-wise constants:

$$E_e^{(i)}(\mathbf{d}_e^{(i)}) = \frac{1}{L_e^{(i)}} \left( L_e^{(i)} + \Delta u_{0,e}^{(i)} \right) \cos \beta_e^{(i)} - \frac{1}{L_e^{(i)}} \Delta w_{0,e}^{(i)} \sin \beta_e^{(i)} - 1, \quad (20a)$$

$$\Gamma_e^{(i)}(\mathbf{d}_e^{(i)}) = \frac{1}{L_e^{(i)}} \left( L_e^{(i)} + \Delta u_{0,e}^{(i)} \right) \sin \beta_e^{(i)} + \frac{1}{L_e^{(i)}} \Delta w_{0,e}^{(i)} \cos \beta_e^{(i)}, \quad (20b)$$

$$K_e^{(i)}(\mathbf{d}_e^{(i)}) = \frac{\Delta \varphi_e^{(i)}}{L_e^{(i)}}, \quad (20c)$$

with, e.g.,  $\Delta \varphi_e^{(i)} = \varphi_{e,2}^{(i)} - \varphi_{e,1}^{(i)}$ ,  $\beta_e^{(i)} = \frac{1}{2}(\varphi_{e,1}^{(i)} + \varphi_{e,2}^{(i)})$ , and  $L_e^{(i)}$  denoting the element length. The contribution of the  $e$ -th element to the internal energy simplifies to

$$\Pi_{\text{int},e}^{(i)}(\mathbf{d}_e^{(i)}) = \frac{1}{2} \left( E^{(i)} A^{(i)} E_e^{(i)}(\mathbf{d}_e^{(i)})^2 + G^{(i)} A_s^{(i)} \Gamma_e^{(i)}(\mathbf{d}_e^{(i)})^2 + E^{(i)} I^{(i)} K_e^{(i)}(\mathbf{d}_e^{(i)})^2 \right) L_e^{(i)}. \quad (21)$$

The discretization is completed by enforcing the inter-layer compatibility conditions (2a) at the element nodes,

$$c_{X,j}^{(i,i+1)} = 0, \quad c_{Z,j}^{(i,i+1)} = 0, \quad (22)$$

indexed at the level of a single layer by  $j = 1, 2, \dots, n^e + 1$ , cf. Figure 1, and with

$$c_{X,j}^{(i,i+1)} = u_{0,j}^{(i)} - u_{0,j}^{(i+1)} + \frac{1}{2}(h^{(i)} \sin \varphi_j^{(i)} + h^{(i+1)} \sin \varphi_j^{(i+1)}), \quad (23a)$$

$$c_{Z,j}^{(i,i+1)} = -\frac{1}{2}(h^{(i)} + h^{(i+1)}) + w_{0,j}^{(i)} - w_{0,j}^{(i+1)} + \frac{1}{2}(h^{(i)} \cos \varphi_j^{(i)} + h^{(i+1)} \cos \varphi_j^{(i+1)}). \quad (23b)$$

For later reference, these are introduced in a compact form as

$$\mathbf{c}(\mathbf{d}) = \mathbf{0}, \quad (24)$$

where  $\mathbf{d} = [\mathbf{d}^{(1)}, \mathbf{d}^{(2)}, \mathbf{d}^{(3)}]$  is a  $9(n^e + 1) \times 1$  column matrix of nodal degrees of freedom and  $\mathbf{c}$  collects the  $4(n^e + 1)$  compatibility conditions (22).

## 4 Governing equations

The true nodal displacements  $\mathbf{d}^*$  follow from the minimization of the discretized energy functional

$$\Pi(\mathbf{d}) = \sum_{i=1}^3 \sum_{e=1}^{n^e} \Pi_{\text{int},e}^{(i)}(\mathbf{d}_e^{(i)}) + \Pi_{\text{ext},e}^{(i)}(\mathbf{d}_e^{(i)}), \quad (25)$$

subject to both kinematic constraints and compatibility conditions (22). While the kinematic constraints are dealt with by matrix reduction techniques, e.g. [18, Appendix A], the compatibility is enforced via the Lagrange multipliers [21, 26]. This yields the Lagrangian function in the form

$$\mathcal{L}(\mathbf{d}, \boldsymbol{\lambda}) = \Pi(\mathbf{d}) + \boldsymbol{\lambda}^\top \mathbf{c}(\mathbf{d}) = \Pi(\mathbf{d}) + \sum_{m=1}^{4(n^e+1)} \lambda_m c_m(\mathbf{d}) \quad (26)$$

where  $\boldsymbol{\lambda}$  is a  $4(n^e + 1) \times 1$  matrix storing the corresponding Lagrange multipliers.

The corresponding Karush-Kuhn-Tucker optimality conditions read, e.g. [6, Chapter 14],

$$\nabla_{\mathbf{d}} \mathcal{L}(\mathbf{d}^*, \boldsymbol{\lambda}^*) = \nabla \Pi(\mathbf{d}^*) + \nabla \mathbf{c}(\mathbf{d}^*)^\top \boldsymbol{\lambda}^* = \mathbf{0}, \quad (27a)$$

$$\nabla_{\boldsymbol{\lambda}} \mathcal{L}(\mathbf{d}^*, \boldsymbol{\lambda}^*) = \mathbf{c}(\mathbf{d}^*) = \mathbf{0}, \quad (27b)$$

with  $\nabla$  denoting the gradient operator and  $\nabla_{\bullet}$  designating the partial derivative with respect to variable  $\bullet$ . These represent a system of non-linear equations, to be solved using the Newton iterative scheme.

To that end, we assume that displacements at iteration  $({}^k \mathbf{d}, {}^k \boldsymbol{\lambda})$  are known and search for the iterative correction in the form

$${}^{k+1} \mathbf{d} = {}^k \mathbf{d} + {}^{k+1} \delta \mathbf{d}. \quad (28)$$

The values of  ${}^{k+1} \delta \mathbf{d}$  are obtained by means of the linearized expressions

$$\nabla \Pi({}^{k+1} \mathbf{d}) \approx \nabla \Pi({}^k \mathbf{d}) + \nabla^2 \Pi({}^k \mathbf{d}) {}^{k+1} \delta \mathbf{d}, \quad (29a)$$

$$\mathbf{c}({}^{k+1} \mathbf{d}) \approx \mathbf{c}({}^k \mathbf{d}) + \nabla \mathbf{c}({}^k \mathbf{d}) {}^{k+1} \delta \mathbf{d}, \quad (29b)$$

$$\nabla \mathbf{c}({}^{k+1} \mathbf{d}) \approx \nabla \mathbf{c}({}^k \mathbf{d}) + \nabla^2 \mathbf{c}({}^k \mathbf{d}) {}^{k+1} \delta \mathbf{d}, \quad (29c)$$

which, when introduced into the optimality conditions (27a) and (27b), result in a linear system of equations, cf. [6] and [28],

$$\begin{bmatrix} {}^k \mathbf{K} & {}^k \mathbf{C}^\top \\ {}^k \mathbf{C} & \mathbf{0} \end{bmatrix} \begin{bmatrix} {}^{k+1} \delta \mathbf{d} \\ {}^{k+1} \boldsymbol{\lambda} \end{bmatrix} = - \begin{bmatrix} {}^k \mathbf{f}_{\text{int}} - \mathbf{f}_{\text{ext}} \\ {}^k \mathbf{c} \end{bmatrix}. \quad (30)$$

Here, we employ the short-hand notation

$${}^k \mathbf{K} = \nabla^2 \Pi({}^k \mathbf{d}) + \sum_{m=1}^{4(n^e+1)} {}^k \lambda_m \nabla^2 c_m({}^k \mathbf{d}) = \mathbf{K}_{\text{t}}({}^k \mathbf{d}) + \mathbf{K}_{\lambda}({}^k \mathbf{d}, {}^k \boldsymbol{\lambda}), \quad (31a)$$

$${}^k \mathbf{C} = \nabla \mathbf{c}({}^k \mathbf{d}), \quad (31b)$$

$${}^k \mathbf{f}_{\text{int}} - \mathbf{f}_{\text{ext}} = \nabla \Pi({}^k \mathbf{d}). \quad (31c)$$

It follows from the specific form of the energy function (25) that the stiffness matrix  $\mathbf{K}_{\text{t}}$  and the matrices of internal  $\mathbf{f}_{\text{int}}$  and external forces  $\mathbf{f}_{\text{ext}}$  exhibit the block structure

$$\mathbf{K}_{\text{t}}(\mathbf{d}) = \begin{bmatrix} \mathbf{K}_{\text{t}}^{(1)}(\mathbf{d}^{(1)}) & & \\ & \mathbf{K}_{\text{t}}^{(2)}(\mathbf{d}^{(2)}) & \\ & & \mathbf{K}_{\text{t}}^{(3)}(\mathbf{d}^{(3)}) \end{bmatrix}, \quad \mathbf{f}_{\text{int}} = \begin{bmatrix} \mathbf{f}_{\text{int}}^{(1)} \\ \mathbf{f}_{\text{int}}^{(2)} \\ \mathbf{f}_{\text{int}}^{(3)} \end{bmatrix}, \quad \mathbf{f}_{\text{ext}} = \begin{bmatrix} \mathbf{f}_{\text{ext}}^{(1)} \\ \mathbf{f}_{\text{ext}}^{(2)} \\ \mathbf{f}_{\text{ext}}^{(3)} \end{bmatrix}. \quad (32)$$

For the  $i$ -th layer, these are obtained by the assembly of contributions of the  $e$ -th element [18], provided by

$$\mathbf{f}_{\text{int},e}^{(i)} = \frac{\partial \Pi_{\text{int},e}^{(i)}}{\partial \mathbf{d}_e^{(i)}}, \quad \mathbf{K}_{\text{t},e}^{(i)} = \frac{\partial^2 \Pi_{\text{int},e}^{(i)}}{\partial \mathbf{d}_e^{(i)2}} = \frac{\partial \mathbf{f}_{\text{int},e}^{(i)}}{\partial \mathbf{d}_e^{(i)}}. \quad (33)$$

In order to keep the paper self-contained, explicit expressions for the matrices needed to set up the linearized system (30) are summarized in Appendix A. Termination of the iterative process (30) is driven by two residuals [6, Section 14.1]

$${}^k\eta_1 = \frac{\|{}^k\mathbf{f}_{\text{int}} - \mathbf{f}_{\text{ext}} + {}^k\mathbf{C}^\top {}^k\boldsymbol{\lambda}\|_2}{\|\mathbf{f}_{\text{ext}}\|_2}, \quad {}^k\eta_2 = \frac{\|{}^k\mathbf{c}\|_2}{\min_i h^{(i)}}, \quad (34)$$

quantifying the validity of the first-order optimality conditions (27). This provides the last component of the non-linear iterative solver, the implementation of which is outlined in Algorithm 1.

---

**Algorithm 1:** Conceptual implementation of the Newton method.

---

**Data:** initial displacement  ${}^0\mathbf{d}$ , tolerances  $\epsilon_1$  and  $\epsilon_2$

**Result:**  $\mathbf{d}^*, \boldsymbol{\lambda}^*$

$k \leftarrow 0, {}^0\boldsymbol{\lambda} \leftarrow \mathbf{0}$ , assemble  ${}^k\mathbf{f}_{\text{int}}, {}^k\mathbf{c}$  and  ${}^k\mathbf{C}$

**while** ( ${}^k\eta_1 > \epsilon_1$ ) *or* ( ${}^k\eta_2 > \epsilon_2$ ) **do**

    assemble  ${}^k\mathbf{K}$

    solve for  $({}^{k+1}\delta\mathbf{d}, {}^{k+1}\boldsymbol{\lambda})$  from Eq. (30)

${}^{k+1}\mathbf{d} \leftarrow {}^k\mathbf{d} + {}^{k+1}\delta\mathbf{d}$

    assemble  ${}^k\mathbf{f}_{\text{int}}, {}^k\mathbf{c}$  and  ${}^k\mathbf{C}$

$k \leftarrow k + 1$

$\mathbf{d}^* \leftarrow {}^k\mathbf{d}, \boldsymbol{\lambda}^* \leftarrow {}^k\boldsymbol{\lambda}$

---

## 5 Examples

In this section, the proposed finite element formulation is verified and partially validated against two benchmarks after Aşık and Tescan [2], involving simply supported, Section 5.1, and fixed-end, Section 5.2, three-layer beams subjected to three-point bending. The comparison is based on the centerline deflections and the extreme stress values at the bottom surface of the bottom layer ( $i = 3$ ). The latter are obtained from the element-wise constant strain measures in the form

$$S_e^{(3)} = \mathbf{E}^{(3)} \left( E_e^{(3)} + \frac{1}{2} K_e^{(3)} h^{(3)} \right), \quad (35)$$

cf. Eq. (10) and Eq. (20), and extrapolated to nodes by the least-square method assuming the piecewise linear distribution of stresses, e.g. [11]. Accuracy of our results against reference experimental data is quantified by

$$\eta_{\text{exp}} = \frac{(\bullet)_{\text{exp}} - (\bullet)}{(\bullet)_{\text{exp}}}, \quad (36)$$

and a similar approach is adopted for reference data obtained by analytical model (an) or two-dimensional finite element simulations (num), both from [2].

Results of the finite-strain formulation are complemented with the small-strain version [28] that corresponds to the first iteration of Algorithm 1. For the completeness, we also provide the response of the equivalent monolithic beam of total thickness  $(h^{(1)} + h^{(2)} + h^{(3)})$  and the layered beam corresponding to two independent layers of thicknesses  $h^{(1)}$  and  $h^{(3)}$ , under the assumption of geometric linearity.<sup>1</sup> Note that to avoid confusion with the terminology used for composite structures [21], the layered approximation will be referred to as *two-layer* and the present formulation is denoted as *refined* in what follows.

---

<sup>1</sup>the present section are reproducible with MATLAB<sup>®</sup> scripts available at the arXiv version of this paper.



### 5.1 Simply supported beam

The first example concerns the simply supported beam with a span of 0.8 m and the total length of 1 m, with a symmetric layer setup of 5–0.38–5 mm in thickness. The structure is subject to a concentrated force at the mid-span ranging from 50 to 200 N and the quantities of interest are registered at the bottom layer, cf. Figure 3(a). The material data for individual layers appear in Table 1. The problem was discretized with  $n^e = 40$  elements per layer (half if symmetry is exploited), in order to achieve the four-digit accuracy of the mid-span deflection for  $F = 200$  N, and the tolerances of the iterative solver were set to  $\epsilon_1 = \epsilon_2 = 10^{-6}$ .

Table 1: Material data for simply supported beam, after [2].

Property	Value
Young's modulus of glass, $E^{(1)} = E^{(3)}$	64.5 GPa
Shear modulus of glass, $G^{(1)} = G^{(3)}$	26.2 GPa
Young's modulus of PVB, $E^{(2)}$	3.61 MPa
Shear modulus of PVB, $G^{(2)}$	1.28 MPa

The centerline deflections as predicted by the considered models appear in Figure 3(b). In this case, the deflection of the refined formulation remains bounded by the two-layer and monolithic cases. The response of the laminated structure is in fact closer to the monolithic beam than to the layered approximation, thereby demonstrating that the interlayer provides sufficient coupling to achieve the composite action. We also observe, in agreement with assumptions of many analytical models discussed in Section 1, the absence of non-linear effects due to statically-determinate character of the test.

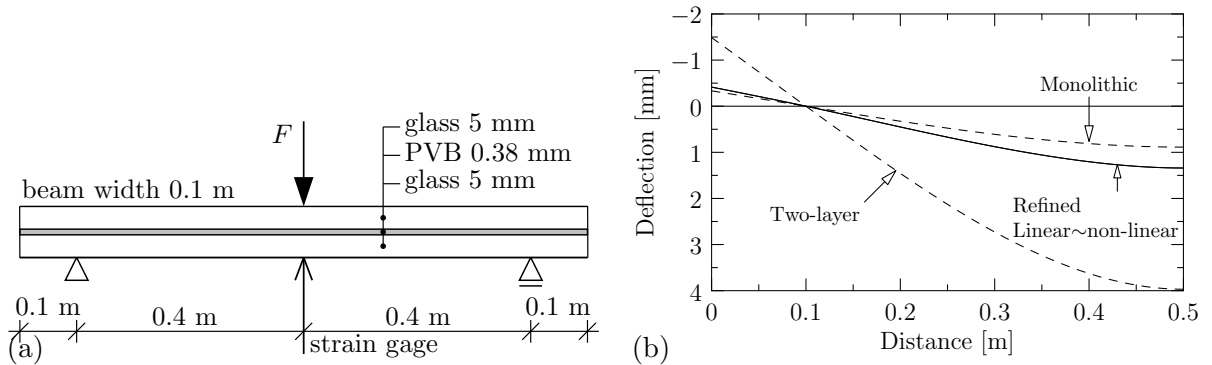


Figure 3: Simply supported three-layer beam; (a) experiment setup and (b) centerline deflections for  $F = 50$  N.

These findings are further supported by Table 2 collecting the numerical values of mid-span deflections and experimental data. The results confirm that predictions of the numerical scheme are in a perfect agreement with the analytical model and correlate well with the experimental data. The limit cases, on the other hand, are too apart to be of practical use and exhibit errors that far exceed the difference between the refined models and experiments.

The response of the structure to an increasing force expressed in the terms of the deflections and stresses appears in Tables 3 and 4, respectively. The data clearly demonstrate that the response of the structure remains linear even for larger loading; the differences appear only for  $F = 200$  N and are indeed negligible. The deflections remain sufficiently accurate with respect to both the analytical model and experiments, while stress values display larger discrepancies. We attribute the  $\sim 1.3\%$  difference between the analytical and numerical models to the fact that Aşık and Tescan in [2] assume glass to deform exclusively in bending and the PVB layer in shear only, while the present approach accounts for both effects simultaneously in all layers.

Table 2: Mid-span deflections  $w_0^{(3)}$  at  $X^{(3)} = L/2$  for the simply supported beam subjected to  $F = 50$  N.

Model	Deflection [mm]	$\eta_{\text{exp}}$ [%]	$\eta_{\text{an}}$ [%]
Experiment <sup>[2]</sup>	1.27	×	-5.2
Analytical model <sup>[2]</sup>	1.34	5.5	×
Laminated linear	1.34	5.6	0.1
Laminated non-linear	1.34	5.6	0.1
Monolithic	0.89	-30.1	-33.8
Layered	3.97	213	196

This error is still significantly smaller compared to the one measured against the experimental data. This might be attributed to inaccuracies in the experiment as explained in detail in [2].

Table 3: Comparison of mid-span deflections  $w_0^{(3)}$  at  $X^{(3)} = L/2$  for the simply supported beam.

Load [N]	Reference data <sup>[2]</sup>		Linear model			Non-linear model		
	$w_{\text{exp}}$ [mm]	$w_{\text{an}}$ [mm]	$w$ [mm]	$\eta_{\text{exp}}$ [%]	$\eta_{\text{an}}$ [%]	$w$ [mm]	$\eta_{\text{exp}}$ [%]	$\eta_{\text{an}}$ [%]
50	1.27	1.34	1.34	5.6	0.1	1.34	5.6	0.1
100	2.55	2.69	2.68	5.2	-0.3	2.68	5.1	-0.3
150	4.12	4.03	4.02	-2.3	-0.1	4.02	-2.5	-0.3
200	5.57	5.38	5.37	-3.7	-0.3	5.35	-4.0	-0.6

Table 4: Comparison of extreme stresses  $S^{(3)}$  at  $X^{(3)} = L/2$  for the simply supported beam.

Load [N]	Reference data <sup>[2]</sup>		Linear model			Non-linear model		
	$S_{\text{exp}}$ [MPa]	$S_{\text{an}}$ [MPa]	$S$ [MPa]	$\eta_{\text{exp}}$ [%]	$\eta_{\text{an}}$ [%]	$S$ [MPa]	$\eta_{\text{exp}}$ [%]	$\eta_{\text{an}}$ [%]
50	9.55	7.23	7.14	-25.3	-1.3	7.14	-25.2	-1.3
100	12.34	14.45	14.27	15.6	-1.3	14.28	15.7	-1.2
150	21.89	21.68	21.40	-2.2	-1.3	21.42	-2.2	-1.2
200	26.27	28.90	28.53	8.6	-1.3	28.55	8.7	-1.2

## 5.2 Fixed-end beam

Effects of geometric non-linearity are illustrated by means of a thin 1.5 m long three-layer beam of thicknesses 2.12–0.76–2.12 mm subjected to a concentrated force at the mid-span with intensity ranging from 15 to 150 N, Figure 5.2(a). The tolerances for the Newton method were set to the same value as in the previous example, and so were the material constants for the glass layers. For the PVB interlayer, we used  $E^{(2)} = 2.8$  MPa and  $G^{(2)} = 1$  MPa. The reference data from [2] include the results of the analytical model, obtained by a finite-difference iterative solver [1], and of detailed two-dimensional large-deformation finite element simulations. To make a direct comparison to these values, we employ the same number of elements per layer,  $n^e = 150$ , but analogous results are obtained for coarser discretizations.

The centerline deflections for geometrically linear and non-linear refined beam formulations appear in Figure 5.2(b) and are compared with the response of equivalent monolithic and two-layer formulations. While the response of the linear model still falls within the monolithic–two-layer bounds (with a closer proximity to the monolithic beam), the deflection of the fully non-linear model is considerably smaller than for the monolithic case. Moreover, the gap between the monolithic and two-layer cases becomes even more pronounced than in the previous example.

The detailed numerical values presented in Table 5 further support our findings. We see that the layered assumption as well as small-strain hypothesis are too conservative and lead to highly inefficient designs, as their errors exceed 100%. The accuracy of the monolithic approximation

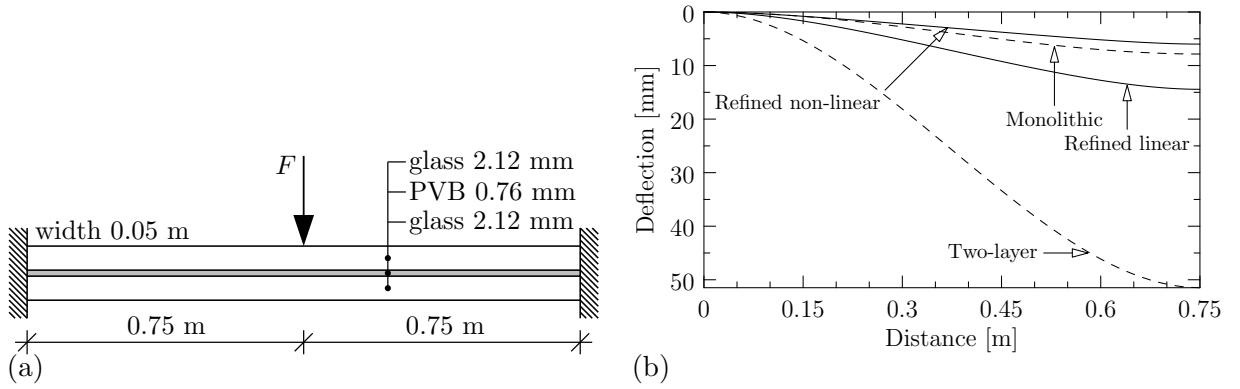


Figure 4: Fixed-end three-layer beam; (a) experiment setup and (b) centerline deflection for  $F = 15$  N.

Table 5: Mid-span deflections  $w_0^{(3)}$  at  $X^{(3)} = L/2$  for the fixed beam subjected to  $F = 15$  N.

Model	Deflection [mm]	$\eta_{\text{num}}$ [%]	$\eta_{\text{an}}$ [%]
2D finite element model <sup>[2]</sup>	5.92	×	0.0
Analytical model <sup>[2]</sup>	5.92	0.0	×
Laminated linear	14.44	144	144
Laminated non-linear	6.00	1.3	1.3
Monolithic	7.85	32.6	32.6
Layered	51.48	770	770

is comparable to the simply supported setup.

Basically the same conclusions follow from the response of the structure to an increasing load, Tables 6 and 7. For the largest load of  $F = 150$  N, the error of the linear laminated model reaches  $\sim 800\%$  for the deflections and  $\sim 250\%$  for the extreme stresses. The finite-strain formulation remains accurate in the whole range of loading, and the errors with respect to the detailed two-dimensional finite element model do not up-cross  $\sim 1\%$  for the deflections and  $\sim 2\%$  for stresses. In fact, it slightly outperforms the analytical model [2] in terms of the stress values, probably due to the more refined representation of the deformation in individual layers as discussed above.

As the final check of our implementation, in Table 8 we present the convergence progress for the load level  $F = 150$  N. In order to investigate reliability of the method, we expose the structure to the full load, instead of applying it incrementally as in [2]. The results confirm significant degree of non-linearity in the structural response. After the first iteration, corresponding to the linear model, the structure is in an out-of-equilibrium state and the layer compatibility is violated. In the following iterations, the residuals are gradually reduced until the ninth iteration, after which the method exhibits quadratic convergence in the equilibrium residual  $\eta_1$  and super-linear convergence in the compatibility residual  $\eta_2$ . This is in a full agreement with available results for the Newton method, e.g. [6, Theorem 13.6], and also explains the convergence difficulties of the heuristic finite-difference solver reported in [2].

## 6 Conclusions

In this paper, we have presented an efficient approach to the analysis of the laminated glass beams. Based on the Mau theory for layered structures, it treats each layer separately and enforces the inter-layer compatibility by the Lagrange multipliers. In our implementation, we utilize a reliable finite element formulation of the Reissner finite-strain beam theory due to Ibrahimbegović and Frey to discretize individual layers, and solve the resulting system of

Table 6: Comparison of mid-span deflections  $w_0^{(3)}$  at  $X^{(3)} = L/2$  for the fixed-end beam.

Load [N]	Reference data <sup>[2]</sup>		Linear model			Non-linear model		
	$w_{an}$ [mm]	$w_{num}$ [mm]	$w$ [mm]	$\eta_{an}$ [%]	$\eta_{num}$ [%]	$w$ [mm]	$\eta_{an}$ [%]	$\eta_{num}$ [%]
15	5.92	5.92	14.44	143.9	143.9	6.00	1.3	1.3
30	8.10	8.10	28.88	256.6	256.6	8.17	0.8	0.8
45	9.60	9.60	43.32	351.3	351.3	9.66	0.6	0.6
60	10.78	10.78	57.76	435.9	435.9	10.83	0.5	0.5
90	12.64	12.63	86.65	585.5	586.0	12.68	0.3	0.4
120	14.10	14.09	115.53	719.4	719.9	14.14	0.3	0.3
150	15.34	15.32	144.41	841.4	842.6	15.36	0.1	0.3

Table 7: Comparison of extreme stresses  $S^{(3)}$  at  $X^{(3)} = L/2$  for the fixed-end beam.

Load [N]	Reference data <sup>[2]</sup>		Linear model			Non-linear model		
	$S_{an}$ [MPa]	$S_{num}$ [MPa]	$S$ [MPa]	$\eta_{an}$ [%]	$\eta_{num}$ [%]	$S$ [MPa]	$\eta_{an}$ [%]	$\eta_{num}$ [%]
15	12.87	12.46	19.50	51.5	56.5	12.60	-2.1	1.1
30	20.69	19.89	38.98	88.4	96.0	20.12	-2.7	1.2
45	27.13	25.94	58.44	115.4	125.3	26.28	-3.2	1.3
60	32.82	31.25	77.88	137.3	149.2	31.69	-3.4	1.4
90	42.82	40.51	116.69	172.5	188.1	41.18	-3.8	1.6
120	51.68	48.64	155.43	200.8	219.6	49.53	-4.2	1.8
150	59.76	56.00	194.10	224.8	246.6	57.13	-4.4	2.0

equations iteratively by the Newton method with consistent linearization. On the basis of the performed simulations, we conjecture that

- in the absence of membrane effects, the formulation reduces exactly to the small-strain model introduced in our previous work,
- although the discretization is based on the lowest-order polynomial basis functions, the method provides results with accuracy comparable to the detailed two-dimensional large-strain finite element simulations,
- the Newton method exhibits a reliable super-linear convergence even for high degrees of non-linearity.

Extension of the current framework to include temperature- and time-dependent properties of the interlayer will be reported independently.

**Acknowledgments** The authors thank Professor Jiří Šejnoha of CTU in Prague for his helpful comments on the original manuscript. This work was supported by the Czech Science Foundation, projects No. P105/12/0331 (AZ) and No. P105/11/0224 (MŠ), and by the Grant Agency of the Czech Technical University in Prague, project No. SGS13/034/OHK1/1T/11 (JZ, MŠ). In addition, JZ acknowledges the partial support of the European Regional Development Fund under the IT4Innovations Centre of Excellence, project No. CZ.1.05/1.1.00/02.0070.

## References

- [1] M. Z. Aşık. Laminated glass plates: revealing of nonlinear behavior. *Computers & Structures*, 81(28–29):2659–2671, 2003.
- [2] M. Z. Aşık and S. Tezcan. A mathematical model for the behavior of laminated glass beams. *Computers & Structures*, 83(21–22):1742–1753, 2005.

Table 8: Convergence of residuals for  $F = 150$  N.

Iteration $k$	$^k\eta_1$	$^k\eta_2$
1	$8.49 \times 10^2$	$7.94 \times 10^{-1}$
2	$1.50 \times 10^3$	$4.65 \times 10^{-1}$
3	$1.02 \times 10^2$	$6.12 \times 10^{-2}$
4	$2.07 \times 10^2$	$5.61 \times 10^{-2}$
5	$2.31 \times 10^1$	$1.11 \times 10^{-2}$
6	$2.43 \times 10^1$	$7.53 \times 10^{-3}$
7	$4.93 \times 10^0$	$2.58 \times 10^{-3}$
8	$1.41 \times 10^0$	$8.17 \times 10^{-4}$
9	$1.38 \times 10^{-1}$	$8.23 \times 10^{-5}$
10	$1.58 \times 10^{-3}$	$8.33 \times 10^{-7}$
11	$2.53 \times 10^{-7}$	$1.18 \times 10^{-10}$

- [3] R. A. Behr, J. E. Minor, M. P. Linden, and C. V. G Vallabhan. Laminated glass units under uniform lateral pressure. *Journal of Structural Engineering*, 111(5):1037–1050, 1985.
- [4] R. A. Behr, J. E. Minor, and H. S. Norville. Structural behavior of architectural laminated glass. *Journal of Structural Engineering*, 119(1):202–222, 1993.
- [5] S. J. Bennison, A. Jagota, and C. A. Smith. Fracture of Glass/Poly(vinyl butyral) (Butacite®) laminates in biaxial flexure. *Journal of the American Ceramic Society*, 82(7):1761–1770, 1999.
- [6] J. F. Bonnans, J. C. Gilbert, C. Lemaréchal, and C. A. Sagastizábal. *Numerical Optimization: Theoretical and Practical Aspects*. Springer, 2003.
- [7] P. Foraboschi. Behavior and failure strength of laminated glass beams. *Journal of Engineering Mechanics*, 133(12):1290–1301, 2007.
- [8] L. Galuppi and G. F. Royer-Carfagni. Effective thickness of laminated glass beams: New expression via a variational approach. *Engineering Structures*, 38:53–67, 2012.
- [9] L. Galuppi and G. F. Royer-Carfagni. Laminated beams with viscoelastic interlayer. *International Journal of Solids and Structures*, 49(18):2637–2645, 2012.
- [10] M. Haldimann, A. Luible, and M. Overend. *Structural Use of Glass*, volume 10 of *Structural Engineering Documents*. IABSE, Zürich, Switzerland, 2008.
- [11] E. Hinton and J. S. Campbell. Local and global smoothing of discontinuous finite element functions using a least squares method. *International Journal for Numerical Methods in Engineering*, 8(3):461–480, 1974.
- [12] J.A Hooper. On the bending of architectural laminated glass. *International Journal of Mechanical Sciences*, 15(4):309–323, 1973.
- [13] A. Ibrahimbegović and A. Delaplace. Microscale and mesoscale discrete models for dynamic fracture of structures built of brittle material. *Computers & Structures*, 81(12):1255–1265, 2003.
- [14] A. Ibrahimbegović and F. Frey. Finite element analysis of linear and non-linear planar deformations of elastic initially curved beams. *International Journal for Numerical Methods in Engineering*, 36(19):3239–3258, 1993.

- [15] A. Ibrahimbegović, C. Knopf-Lenoir, A. Kučerová, and P. Villon. Optimal design and optimal control of structures undergoing finite rotations and elastic deformations. *International Journal for Numerical Methods in Engineering*, 61(14):2428–2460, 2004, 0902.1665.
- [16] H. Irschik and J. Gerstmayr. A continuum mechanics based derivation of Reissner’s large-displacement finite-strain beam theory: the case of plane deformations of originally straight Bernoulli-Euler beams. *Acta Mechanica*, 206(1):1–21, 2009.
- [17] I. V. Ivanov. Analysis, modelling, and optimization of laminated glasses as plane beam. *International Journal of Solids and Structures*, 43(22–23):6887–6907, 2006.
- [18] M. Jirásek and Z. P. Bažant. *Inelastic analysis of structures*. John Wiley & Sons, Ltd., 2002.
- [19] J. Kruis, K. Matouš, and Z. Dostál. Solving laminated plates by domain decomposition. *Advances in Engineering Software*, 33(7–10):445–452, 2002.
- [20] A. Kučerová. Optimisation de forme et contrôle de chargement des structures elastique soumis de rotation finis en utilisant les algorithmes génétiques. Master’s thesis, Ecole Normale Supérieure de Cachan, 2003. Available at [http://klobouk.fsv.cvut.cz/~anicka/publications/DEA\\_MaiSE\\_2003.pdf](http://klobouk.fsv.cvut.cz/~anicka/publications/DEA_MaiSE_2003.pdf).
- [21] S. T. Mau. A refined laminated plate theory. *Journal of Applied Mechanics–Transactions of the ASME*, 40(2):606–607, 1973.
- [22] H. S. Norville, K. W. King, and J. L. Swofford. Behavior and strength of laminated glass. *Journal of Engineering Mechanics*, 124(1):46–53, 1998.
- [23] E. Reissner. On one-dimensional finite-strain beam theory: the plane problem. *Journal of Applied Mathematics and Physics*, 23(5):795–804, 1972.
- [24] S.-H. Schulze, M. Pander, K. Naumenko, and H. Altenbach. Analysis of laminated glass beams for photovoltaic applications. *International Journal of Solids and Structures*, 49(15–16):2027–2036, 2012.
- [25] G. Sedlacek, K. Blank, and J. Guesgen. Glass in structural engineering. *Structural Engineer*, 73(2):17–22, 1995.
- [26] M. Šejnoha. Initial failure of unidirectional fiber reinforced laminates subjected to bending. *Building Research Journal*, 48(1):31–41, 2000.
- [27] C. V. G. Vallabhan, J. E. Minor, and S. R. Nagalla. Stress in layered glass units and monolithic glass plates. *Journal of Structural Engineering*, 113:36–43, 1987.
- [28] A. Zemanová, J. Zeman, and M. Šejnoha. Simple numerical model of laminated glass beams. *Acta Polytechnica*, 48(6):22–26, 2008, 1201.3479.

## A Sensitivity analysis

The expression for the internal nodal forces follows directly from Eq. (33)<sub>1</sub>. After certain manipulations we arrive at, cf. [20]

$$\mathbf{f}_{\text{int},e}^{(i)} = \begin{bmatrix} f_{\text{int},e,1}^{(i)} \\ f_{\text{int},e,2}^{(i)} \\ f_{\text{int},e,3}^{(i)} \\ f_{\text{int},e,4}^{(i)} \\ f_{\text{int},e,5}^{(i)} \\ f_{\text{int},e,6}^{(i)} \end{bmatrix} = \begin{bmatrix} -E^{(i)} A^{(i)} E_e^{(i)} \cos \beta_e^{(i)} - G^{(i)} A_s^{(i)} \Gamma_e^{(i)} \sin \beta_e^{(i)} \\ E^{(i)} A^{(i)} E_e^{(i)} \sin \beta_e^{(i)} - G^{(i)} A_s^{(i)} \Gamma_e^{(i)} \cos \beta_e^{(i)} \\ -\frac{1}{2}(L_e^{(i)} + \Delta u_{0,e}^{(i)}) f_{\text{int},e,2}^{(i)} + \frac{1}{2} \Delta w_{0,e}^{(i)} f_{\text{int},e,1}^{(i)} - E^{(i)} I^{(i)} K_e^{(i)} \\ -f_{\text{int},e,1}^{(i)} \\ -f_{\text{int},e,2}^{(i)} \\ -\frac{1}{2}(L_e^{(i)} + \Delta u_{0,e}^{(i)}) f_{\text{int},e,2}^{(i)} + \frac{1}{2} \Delta w_{0,e}^{(i)} f_{\text{int},e,1}^{(i)} + E^{(i)} I^{(i)} K_e^{(i)} \end{bmatrix}. \quad (37)$$

By an analogous procedure one obtains from Eq. (33)<sub>2</sub>

$$\mathbf{K}_{t,e}^{(i)} = \begin{bmatrix} K_{t,e,11}^{(i)} & K_{t,e,12}^{(i)} & K_{t,e,13}^{(i)} & -K_{t,e,11}^{(i)} & -K_{t,e,12}^{(i)} & K_{t,e,13}^{(i)} \\ K_{t,e,12}^{(i)} & K_{t,e,22}^{(i)} & K_{t,e,23}^{(i)} & -K_{t,e,12}^{(i)} & -K_{t,e,22}^{(i)} & K_{t,e,23}^{(i)} \\ K_{t,e,13}^{(i)} & K_{t,e,23}^{(i)} & K_{t,e,33}^{(i)} & -K_{t,e,13}^{(i)} & -K_{t,e,23}^{(i)} & K_{t,e,36}^{(i)} \\ -K_{t,e,11}^{(i)} & -K_{t,e,12}^{(i)} & -K_{t,e,13}^{(i)} & K_{t,e,11}^{(i)} & K_{t,e,12}^{(i)} & -K_{t,e,13}^{(i)} \\ -K_{t,e,12}^{(i)} & -K_{t,e,22}^{(i)} & -K_{t,e,23}^{(i)} & K_{t,e,12}^{(i)} & K_{t,e,22}^{(i)} & -K_{t,e,23}^{(i)} \\ K_{t,e,13}^{(i)} & K_{t,e,23}^{(i)} & K_{t,e,36}^{(i)} & -K_{t,e,13}^{(i)} & -K_{t,e,23}^{(i)} & K_{t,e,33}^{(i)} \end{bmatrix}, \quad (38)$$

where the individual entries read

$$\begin{aligned} K_{t,e,11}^{(i)} &= \frac{\partial f_{\text{int},e,1}^{(i)}}{\partial u_{0,e,1}^{(i)}} = \frac{1}{L_e^{(i)}} \left( E^{(i)} A^{(i)} \cos^2 \beta_e^{(i)} + G^{(i)} A_s^{(i)} \sin^2 \beta_e^{(i)} \right), \\ K_{t,e,12}^{(i)} &= \frac{\partial f_{\text{int},e,1}^{(i)}}{\partial w_{0,e,1}^{(i)}} = \frac{1}{2L_e^{(i)}} \left( -E^{(i)} A^{(i)} + G^{(i)} A_s^{(i)} \right) \sin 2\beta_e^{(i)}, \\ K_{t,e,13}^{(i)} &= \frac{\partial f_{\text{int},e,1}^{(i)}}{\partial \varphi_{e,1}^{(i)}} = \frac{1}{2} \left[ \left( E^{(i)} A^{(i)} - G^{(i)} A_s^{(i)} \right) \left( E_e^{(i)} \sin \beta_e^{(i)} + \Gamma_e^{(i)} \cos \beta_e^{(i)} \right) - G^{(i)} A_s^{(i)} \sin \beta_e^{(i)} \right], \\ K_{t,e,22}^{(i)} &= \frac{\partial f_{\text{int},e,2}^{(i)}}{\partial w_{0,e,1}^{(i)}} = \frac{1}{L_e^{(i)}} \left( E^{(i)} A^{(i)} \sin^2 \beta_e^{(i)} + G^{(i)} A_s^{(i)} \cos^2 \beta_e^{(i)} \right), \\ K_{t,e,23}^{(i)} &= \frac{\partial f_{\text{int},e,2}^{(i)}}{\partial \varphi_{e,1}^{(i)}} = \frac{1}{2} \left[ \left( E^{(i)} A^{(i)} - G^{(i)} A_s^{(i)} \right) \left( E_e^{(i)} \cos \beta_e^{(i)} - \Gamma_e^{(i)} \sin \beta_e^{(i)} \right) - G^{(i)} A_s^{(i)} \cos \beta_e^{(i)} \right], \\ K_{t,e,33}^{(i)} &= \frac{\partial f_{\text{int},e,3}^{(i)}}{\partial \varphi_{e,1}^{(i)}} = \frac{1}{2} \left[ - \left( L_e^{(i)} + \Delta u_{0,e}^{(i)} \right) K_{t,e,23}^{(i)} + \Delta w_{0,e}^{(i)} K_{t,e,13}^{(i)} \right] + \frac{E^{(i)} I^{(i)}}{L_e^{(i)}}, \\ K_{t,e,36}^{(i)} &= \frac{\partial f_{\text{int},e,3}^{(i)}}{\partial \varphi_{e,2}^{(i)}} = K_{t,e,33}^{(i)} - \frac{2E^{(i)} I^{(i)}}{L_e^{(i)}}. \end{aligned}$$

The remaining terms in the system (30) originate from the compatibility conditions (22). In particular, the matrix  $\mathbf{C}$  is analogous to the small-strain tying condition [28, Section 4]. The block of  $\mathbf{C}$ , associated with a node  $j$  and layers  $i$  and  $(i+1)$  attains the form

$$\mathbf{C}_j^{(i,i+1)} = \begin{bmatrix} 1 & 0 & \frac{1}{2} h^{(i)} \cos \varphi_j^{(i)} & \cdots & -1 & 0 & \frac{1}{2} h^{(i+1)} \cos \varphi_j^{(i+1)} \\ 0 & 1 & -\frac{1}{2} h^{(i)} \sin \varphi_j^{(i)} & \cdots & 0 & -1 & -\frac{1}{2} h^{(i+1)} \sin \varphi_j^{(i+1)} \end{bmatrix}. \quad (39)$$

The second derivatives of the compatibility conditions quantify their contributions to the tangent stiffness

$$\mathbf{K}_{\lambda,j}^{(i,i+1)} = \frac{\partial^2 c_X^{(i,i+1)}}{\partial \mathbf{d}_j^{(i,i+1)2}} \lambda_{X,j}^{(i,i+1)} + \frac{\partial^2 c_Z^{(i,i+1)}}{\partial \mathbf{d}_j^{(i,i+1)2}} \lambda_{Z,j}^{(i,i+1)}. \quad (40)$$

This additional term is expressed as

$$\mathbf{K}_{\lambda,j}^{(i,i+1)} = \begin{bmatrix} 0 & 0 & 0 & \cdots & 0 & 0 & 0 \\ 0 & 0 & 0 & \cdots & 0 & 0 & 0 \\ 0 & 0 & K_{\lambda,\varphi_j^{(i)}}^{(i,i+1)} & \cdots & 0 & 0 & 0 \\ \vdots & \vdots & \vdots & \ddots & \vdots & \vdots & \vdots \\ 0 & 0 & 0 & \cdots & 0 & 0 & 0 \\ 0 & 0 & 0 & \cdots & 0 & 0 & 0 \\ 0 & 0 & 0 & \cdots & 0 & 0 & K_{\lambda,\varphi_j^{(i+1)}}^{(i,i+1)} \end{bmatrix}, \quad (41)$$

with non-zero entries provided by

$$K_{\lambda,\varphi_j^{(i)}}^{(i,i+1)} = -\frac{1}{2}h^{(i)}(\sin \varphi_j^{(i)} \lambda_{X,j}^{(i,i+1)} + \cos \varphi_j^{(i)} \lambda_{Z,j}^{(i,i+1)}), \quad (42a)$$

$$K_{\lambda,\varphi_j^{(i+1)}}^{(i,i+1)} = -\frac{1}{2}h^{(i+1)}(\sin \varphi_j^{(i+1)} \lambda_{X,j}^{(i,i+1)} + \cos \varphi_j^{(i+1)} \lambda_{Z,j}^{(i,i+1)}). \quad (42b)$$